IUCrJ

Grazing-incidence small-angle X-ray scattering (GISAXS) on small periodic targets using large beams. Erratum

Mika Pflüger,[a]* Victor Soltwisch,[a] Jürgen Probst,[b] Frank Scholze[a] and Michael Krumrey[a]

[a]Physikalisch-Technische Bundesanstalt (PTB), Abbestraße 2-12, 10587 Berlin, Germany, and [b]Helmholtz-Zentrum Berlin (HZB), Albert-Einstein-Straße 15, 12489 Berlin, Germany. *Correspondence e-mail: mika.pflueger@ptb.de

An error in the paper by Pflüger, Soltwisch, Probst, Scholze & Krumrey [*IUCrJ* (2017), 431–438] is corrected.
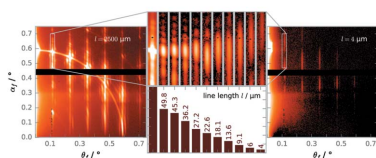
In the article by Pflüger *et al.* (2017), there is an error in equation (5) (§2, p. 433). The arcsin function should be arctan.

The corrected equation thus reads

$$\theta_{\mathrm{f}} = \arctan\left(\frac{\cos\varphi\, n\lambda}{\sin\varphi\, n\lambda + p\cos\alpha_{\mathrm{i}}}\right). \tag{5}$$

References

Pflüger, M., Soltwisch, V., Probst, J., Scholze, F. & Krumrey, M. (2017). *IUCrJ*, **4**, 431–438.

OPEN ACCESS

IUCrJ

Grazing-incidence small-angle X-ray scattering (GISAXS) on small periodic targets using large beams

Mika Pflüger,[a]* Victor Soltwisch,[a] Jürgen Probst,[b] Frank Scholze[a] and Michael Krumrey[a]

[a]Physikalisch-Technische Bundesanstalt (PTB), Abbestraße 2-12, 10587 Berlin, Germany, and [b]Helmholtz-Zentrum Berlin (HZB), Albert-Einstein-Straße 15, 12489 Berlin, Germany. *Correspondence e-mail: mika.pflueger@ptb.de

Grazing-incidence small-angle X-ray scattering (GISAXS) is often used as a versatile tool for the contactless and destruction-free investigation of nano-structured surfaces. However, due to the shallow incidence angles, the footprint of the X-ray beam is significantly elongated, limiting GISAXS to samples with typical target lengths of several millimetres. For many potential applications, the production of large target areas is impractical, and the targets are surrounded by structured areas. Because the beam footprint is larger than the targets, the surrounding structures contribute parasitic scattering, burying the target signal. In this paper, GISAXS measurements of isolated as well as surrounded grating targets in Si substrates with line lengths from 50 µm down to 4 µm are presented. For the isolated grating targets, the changes in the scattering patterns due to the reduced target length are explained. For the surrounded grating targets, the scattering signal of a 15 µm × 15 µm target grating structure is separated from the scattering signal of 100 µm × 100 µm nanostructured surroundings by producing the target with a different orientation with respect to the predominant direction of the surrounding structures. As virtually all litho-graphically produced nanostructures have a predominant direction, the described technique allows GISAXS to be applied in a range of applications, e.g. for characterization of metrology fields in the semiconductor industry, where up to now it has been considered impossible to use this method due to the large beam footprint.

1. Introduction

For the investigation of nanostructured surfaces, grazing-incidence small-angle X-ray scattering (GISAXS) is now established as a powerful technique (Hexemer & Müller-Buschbaum, 2015; Renaud *et al.*, 2009). For example, GISAXS is used to investigate the active layer of solar cells *ex situ* as well as *in situ* (Gu *et al.*, 2012; Müller-Buschbaum, 2014; Rossander *et al.*, 2014; Pröller *et al.*, 2016), surface and bulk morphology of polymer films (Müller-Buschbaum, 2003; Wernecke *et al.*, 2014a), surface roughness and roughness correlations (Holý *et al.*, 1993; Holý & Baumbach, 1994; Babonneau *et al.*, 2009), lithographically produced structures (Gollmer *et al.*, 2014; Soccio *et al.*, 2015) and deposition growth kinetics (Lairson *et al.*, 1995; Renaud *et al.*, 2003). GISAXS offers non-destructive contact-free measurements of sample structures with feature sizes between about 1 nm and 1 µm, giving statistical information about the whole illuminated volume.

Due to the small incidence angle α_i close to the angle of total external reflection α_c and due to the large number of scatterers in the investigated volume, scattered intensities are

431
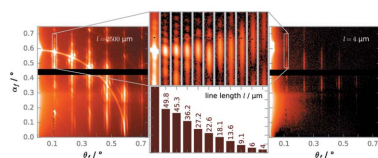
much higher in GISAXS geometry compared with transmission SAXS (Levine *et al.*, 1989). However, the low incidence angle also causes an elongated beam footprint on the sample, leading to large illuminated areas even for small incident beams. For a typical GISAXS incidence angle of $\alpha_i \approx 0.5°$, the footprint on the sample is ~ 100 times longer than the incident beam height. For a moderately small beam of a synchrotron radiation beamline (height $\simeq 500\ \mu m$), the length of the footprint on the sample is thus several centimetres. Due to the long footprints, GISAXS has so far been routinely used only on samples which are at least several millimetres long. To achieve shorter beam footprints, the beam height needs to be reduced. The smallest beam height of about 300 nm used in GISAXS experiments so far (Roth *et al.*, 2007) has led to a footprint on the sample of about 30 μm, but presents large technical challenges in aligning the sample to the beam. However, for many applications, the measurement of very small target areas down to a few micrometres in length is necessary, and the use of laboratory X-ray sources with comparably large beams is desirable. A prominent application where GISAXS has been rejected so far for the mentioned reasons is the characterization of metrology fields in high-volume manufacturing of semiconductors. These fields are surrounded by other structures and larger field sizes directly translate to lost wafer area and thus additional production costs (Bunday, 2016).

One approach to measuring small target areas on a surface is to use SAXS in transmission geometry. Transmission SAXS in principle probes the whole penetrated sample volume, but it can also be used to investigate surfaces if the sample bulk is sufficiently homogeneous (Hu *et al.*, 2004; Sunday *et al.*, 2015), offering a method to investigate small surface areas non-destructively and in a contact-free way. Unfortunately, trans-

mission SAXS is not usable for thick (with respect to the substrate material's absorption length) samples that absorb a large portion of the incoming beam nor for inhomogeneous samples where for example buried layers add to the scattering background. For such samples, measurements in GISAXS geometry would be preferred if the problem of large illuminated areas could be overcome.

We show that GISAXS measurements of micrometre-sized structured surfaces are possible using existing non-focused sources for isolated targets as well as for suitably prepared periodic targets in a periodic environment. The scattering of isolated grating targets with lengths from 4 μm to 50 μm is compared with the scattering of a 2500 μm-long (quasi-infinite) grating target. We explain the length-dependent changes in the scattering patterns using the theory for slit diffraction. For the measurement of targets surrounded by other nanostructures, we produce the grating targets with a different direction with respect to the predominant direction of their surroundings. This allows us to separate the scattering signal of the targets from the signal of the surroundings by aligning the incident X-ray beam to the target.

2. GISAXS at gratings

The measurement geometry of GISAXS (Levine *et al.*, 1989) is shown schematically in Fig. 1. The sample is illuminated under grazing-incidence angle α_i, and the resulting reflected and scattered radiation is collected with an area detector at exit angles α_f and θ_f. We chose our coordinate system such that the x–y-plane is the sample plane and the x-axis lies in the scattering plane, with the z-axis perpendicular to the sample plane. In this coordinate system, the scattering vector $\mathbf{q} = \mathbf{k}_f - \mathbf{k}_i$ takes the form

$$q_x = k(\cos\theta_f \cos\alpha_f - \cos\alpha_i), \quad (1)$$

$$q_y = k(\sin\theta_f \cos\alpha_f), \quad (2)$$

$$q_z = k(\sin\alpha_i + \sin\alpha_f), \quad (3)$$

with the wavevector of the incoming beam $\mathbf{k}_i$, the wavevector of the scattered beam $\mathbf{k}_f$, $k = |\mathbf{k}_i| = |\mathbf{k}_f| = 2\pi/\lambda$, and the wavelength of the incident radiation λ.

Several groups have already performed GISAXS measurements on gratings, and the scattering of perfect gratings is well understood. Tolan *et al.* (1995), Metzger *et al.* (1997), Jergel *et al.* (1999) and Mikulík & Baumbach (1999) measured gratings in GISAXS geometry with the grating lines perpendicular to the incoming beam (coplanar geometry). GISAXS measurements with the grating lines along the incoming beam (so-called non-coplanar geometry, conical mounting or sagittal diffraction geometry) were analysed by Mikulík *et al.* (2001). Their paper already contains the reciprocal-space construction of the resulting scattering pattern laid out in detail by Yan & Gibaud (2007). Hofmann *et al.* (2009) reconstructed a simple line profile using the distorted-wave Born approximation (DWBA) formalism. Hlaing *et al.* (2011) examined the production of gratings by nanoimprinting
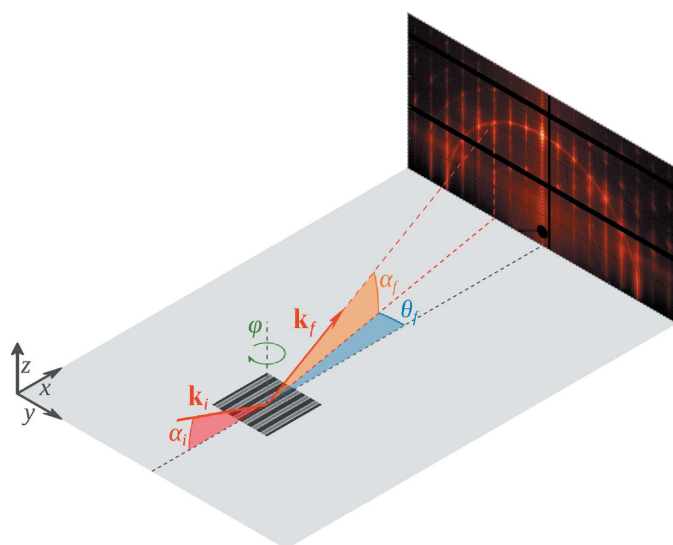

Figure 1
Geometry of GISAXS experiments. A monochromatic X-ray beam with a wavevector $\mathbf{k}_i$ impinges on the sample surface at a grazing-incidence angle α_i. The elastically scattered wavevector $\mathbf{k}_f$ propagates along the exit angle α_f and the azimuthal angle θ_f. The sample can be rotated around the z-axis by the angle φ.

and extracted the side-wall angle of the grating profile. For very rough polymer gratings, where the grating diffraction is not usable for the analysis, Meier *et al.* (2012) could still extract the line profile including the side-wall angle and line width from the diffuse part of the scattering. Measuring rough polymer gratings as well, Rueda *et al.* (2012) use the DWBA formalism with form factors of different length to model gratings with varying roughness. With a different theoretical approach, Wernecke *et al.* (2012, 2014*b*) extracted the line and groove width as well as the line height of gratings using Fourier analysis. Solving the Maxwell equations using finite elements, Soltwisch *et al.* (2014*a*, 2017) reconstructed detailed line profiles of gratings, including a top and bottom corner rounding as well as the side-wall angle, the line width and height. Most recently, Suh *et al.* (2016) measured rough polymer gratings and extracted the average line profile as well as the magnitude of deviations from the average line profile using DWBA. Notably, they also showed that the reconstruction did not improve further when using a more complex line profile shape, thus demonstrating that a relatively simple line shape already describes the X-ray scattering of their grating.

The diffraction of gratings in GISAXS geometry can be described as the intersection of the reciprocal-space representation of the grating and the Ewald sphere of elastic scattering (Mikulík *et al.*, 2001; Yan & Gibaud, 2007). The reciprocal-space representation of a grating periodically extending into infinity in the y-direction with infinite length and vanishing height is an array of rods [so-called grating truncation rods (GTRs)] lying parallel to the reciprocal k_y–k_z-plane (see Fig. 3*a*). The intersection of the GTRs and the Ewald sphere is a series of grating diffraction orders on a semicircle, evenly spaced in k_y, each $2\pi/p$ apart with grating pitch p. If the grating is rotated in the sample plane by the angle φ such that the grating lines are no longer parallel to the x-axis, the GTR plane is rotated around the k_z-axis by φ, so that the scattering pattern becomes asymmetric. At the small incidence angles used in GISAXS, the curvature of the Ewald sphere is very steep at the intersection, leading to large changes in the scattering pattern even for small deviations in φ (Mikulík *et al.*, 2001).

Using the same construction as Yan & Gibaud (2007), but in the coordinate system used in this paper, the positions of the grating diffraction orders are (see supporting information for the derivation)

$$\alpha_f = \arcsin\left\{\left[\sin^2\alpha_i - \left(\frac{n\lambda}{p}\right)^2 - \frac{2n\lambda\sin\varphi\cos\alpha_i}{p}\right]^{1/2}\right\}, \quad (4)$$

$$\theta_f = \arcsin\left(\frac{\cos\varphi\, n\lambda}{\sin\varphi\, n\lambda + p\cos\alpha_i}\right) \quad (5)$$

with the X-ray wavelength λ, the grating diffraction order $n \in \mathbb{Z}$ and the grating pitch p.

3. Instrumentation

3.1. Sample preparation

All structures were fabricated by electron beam lithography on a Vistec EBPG5000+ using positive resist ZEP520A on silicon substrates, followed by reactive ion etching with SF_6 and C_4F_8 and resist stripping with an oxygen plasma treatment (Senn *et al.*, 2011).

3.2. GISAXS experiments

The experiments were conducted at the four-crystal monochromator (FCM) beamline (Krumrey & Ulm, 2001) in the laboratory (Beckhoff *et al.*, 2009) of the Physikalisch-Technische Bundesanstalt (PTB) at the electron storage ring BESSY II. This beamline allows the adjustment of the photon energy in the range from 1.75 keV to 10 keV. By using a beam-defining 0.52 mm-diameter pinhole about 150 cm before the sample position and a scatter guard 1 mm pinhole about 10 cm before the sample, the beam spot size was about 0.5 mm × 0.5 mm at the sample position with minimal parasitic scattering. Both pinholes are low-scatter SCATEX germanium pinholes (Incoatec GmbH, Germany). Alternatively, the beam spot size could be reduced to about 0.1 mm × 0.1 mm by using a beam-defining 100 µm Pt pinhole (Plano GmbH, Germany) and an adjustable slit system with low-scatter blades (XENOCS, France) as a scatter guard. The GISAXS setup at the FCM beamline consists of a sample chamber (Fuchs *et al.*, 1995) and the HZB SAXS setup (Gleber *et al.*, 2010). The sample chamber is equipped with a goniometer which allows sample movements in all directions with a resolution of 3 µm as well as rotations around all sample axes with an angular resolution of 0.001°. The HZB SAXS setup allows moving the in-vacuum Pilatus 1M area detector (Wernecke *et al.*, 2014*c*), reaching sample-to-detector distances from about 2 m to about 4.5 m and exit angles up to about 2°. Due to the single-pixel photon detection of the Pilatus detector, the detector angular resolution for both exit angles α_f and θ_f is given by the solid angle covered by an individual pixel, which is between 0.005° for a sample-to-detector distance of 2 m and 0.002° for a sample-to-detector distance of 4.5 m. Along the whole beam path including the sample site, high vacuum (pressure below 10^{-4} mbar) is maintained.

4. Length series

To test the lower limits of target sizes in GISAXS, we manufactured a series of grating targets on a single silicon wafer, with each target consisting of 40 grooves of differing line length l, forming a grating with pitch $p = 100$ nm. In total, 11 targets were produced in this length series, one 'infinitely' long target with $l = 2500$ µm and ten targets with lengths ranging from $l = 50$ µm down to 4 µm. For all targets, the target width is 4 µm, the individual line width is $w = 55$ nm and the nominal line height is $h = 45$ nm. The targets were placed at a distance of 3.04 mm from their nearest neighbour to ensure that in conical mounting only one target is hit by the beam.
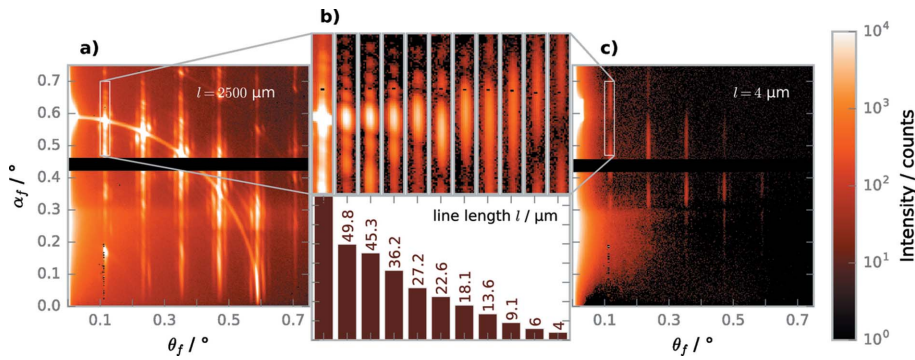
Figure 2
Changes in the GISAXS pattern by line length. (*a*) GISAXS pattern of the 2500 µm-long grating, showing diffraction orders on a circle. (*b*) Detailed view of the first diffraction order of gratings with differing lengths, showing the elongation of the first diffraction order with decreasing grating length (top) and corresponding grating lengths (bottom). (*c*) GISAXS pattern of the 4 µm-long grating, showing the elongated diffraction orders. For comparability, all measurements were taken with the same exposure time, which leads to overexposure for the 2500 µm-long grating.

For the measurements of the very small targets in GISAXS, we need to consider how much of the incoming X-ray beam can interact with the measured target. Due to the shallow incidence angle, the beam footprint on the sample is enlarged by $1/\sin(\alpha_i)$. With a beam size of about 0.5 mm × 0.5 mm and an incidence angle of $\alpha_i = 0.6°$, this yields a beam footprint on the sample of about 0.5 mm × 50 mm. The largest target covers an area of 4 µm × 2500 µm on the substrate, so only $\sim 4 \times 10^{-4}$ of the incident beam interacts with the largest target, and for the smallest target (4 µm × 4 µm) only $\sim 6 \times 10^{-7}$ of the beam hits the target. The scattering from the targets is thus extraordinarily weak and superimposed with the scattering from the surrounding substrate. Using suitably long exposure times of $t = 1$ h with the noise-free single-photon-counting detector, scattering patterns could still be collected. We assume incoherent addition of the scattering of the target grating and the diffuse scattering background of the surrounding surface. By fitting and subtracting the diffuse scattering background (see the supporting information), we obtain scattering patterns of all targets. Measurements for all targets were taken at $E = 6$ keV with an incidence angle of $\alpha_i \simeq 0.6°$ in conical mounting.

While the scattering from the longest grating (Fig. 2*a*) shows sharp diffraction orders on a semicircle similar to the scattering patterns of infinitely long gratings, shorter gratings show length-dependent changes (Fig. 2*b*) and the shortest grating (Fig. 2*c*) produces a scattering pattern which has lost the circle-like interference pattern almost completely. For the small ($l \leq 50$ µm) gratings, side lobes above and below the grating diffraction order are visible, and with decreasing length the diffraction orders as well as the side lobes elongate in the vertical direction and the side lobes move further away from the main peak. The width of the peaks in the horizontal direction does not change with line length l and is due to the size and divergence of the incoming X-ray beam. Additional scattering peaks visible in Fig. 2(*a*) are due to scattering with $q_x \neq 0$ arising from the length of the e-beam writing field of about $\Delta x \simeq 4.53$ µm (Soltwisch *et al.*, 2014*b*).

To explain the changes in the scattering patterns for gratings with finite length, we need to consider the changes in reciprocal space when the grating is finite in the *x*-direction. The finite length enlarges the grating truncation rods in k_x, leading to grating truncation sheets. The intersection of the grating truncation sheets with the Ewald sphere then leads to elongated diffraction orders (see Fig. 3). For a quantitative description of the intensity profile along the diffraction orders, we treat the diffraction from short gratings as single-slit diffraction. The intensity I after diffraction on a single slit is (Meschede, 2015)

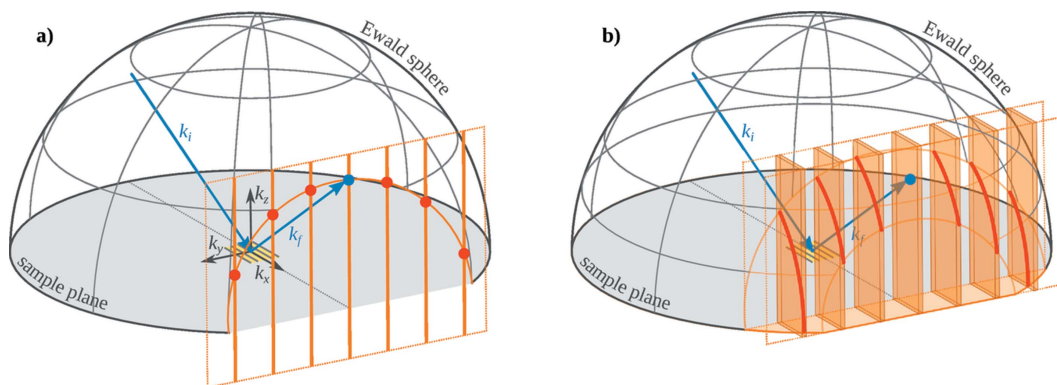$$I = I_0 \left[\mathrm{sinc}\left(\frac{s\pi \sin \beta}{\lambda}\right) \right]^2, \qquad (6)$$

Figure 3
Reciprocal-space construction of GISAXS from gratings. (*a*) Ewald sphere (grey mesh) and grating truncation rods (orange), which are the reciprocal-space representation of an infinite grating. The projection of the intersection (red) on the detector (not shown) leads to the GISAXS pattern. (*b*) For a short (*i.e.* finitely long) grating, the reciprocal-space representation (orange) along k_x is no longer a delta function. Instead, it is $\propto \mathrm{sinc}\, k_x$, leading to grating truncation sheets. The intersection of the grating truncation sheets and the Ewald sphere leads to elongated diffraction orders.

with the unnormalized cardinal sine function $\mathrm{sinc}(x) = \sin(x)/x$ and the intensity factor I_0. In our case, the effective width of the slit s is the projection of the line length on the incoming beam, $s = l \sin \alpha_i$, and the angle of diffraction β is the deviation from the specularly reflected beam, $\beta = \alpha_i - \alpha_f$. For comparison with the experimental data, we solve equation (6) numerically for β by inserting $I = I_0/2$, which yields

$$\mathrm{FWHM} = 2\beta \simeq 2\arcsin\left(\frac{0.443\lambda}{l \sin \alpha_i}\right), \qquad (7)$$

for the full width at half-maximum (FWHM) of the elongated main peak.

We have extracted the FWHM peak width as shown in Figs. 4(b) and 4(c) for all targets in the length series. The
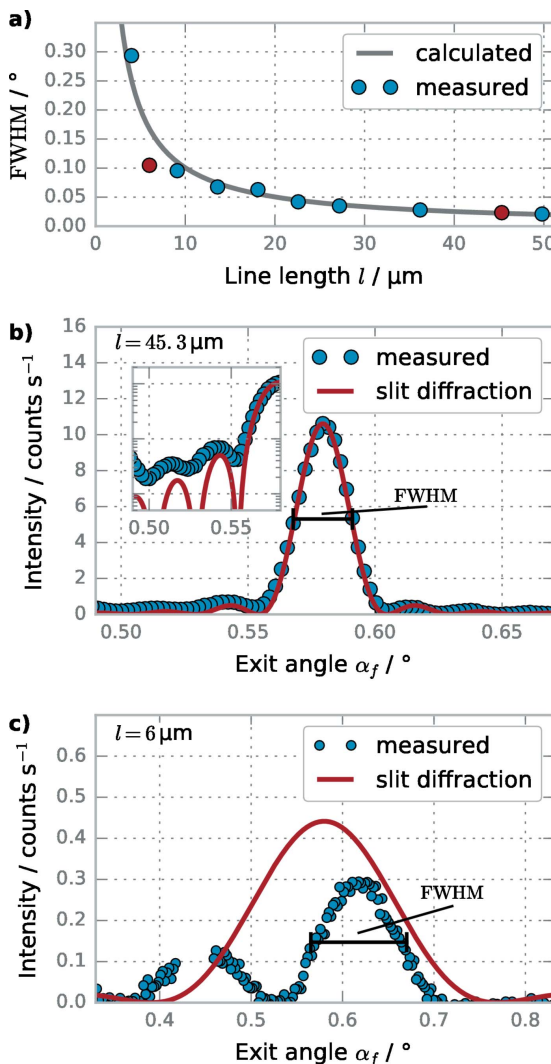

Figure 4
Description of scattering of short gratings as single-slit diffraction. (a) Comparison between the measured FWHM extracted from the GISAXS patterns for the length series and the FWHM calculated from the line length l according to equation (7). The marked red dots correspond to line lengths shown in detail in (b) and (c). (b, c) Cut along the first diffraction order of the scattering of the grating target with $l = 45.3$ μm (b) and $l = 6$ μm (c). What is shown is the FWHM extracted from the measured data and the intensity profile calculated for slit diffraction according to equation (6). The inset in (b) shows the intensity in logarithmic units.

results are shown and compared with the theoretical values from equation (7) in Fig. 4(a). As can be seen in Figs. 4(a) and 4(b), slit diffraction describes the scattering of the targets with long line lengths l very well. Form and width of the main peak are identical for the theoretical description in comparison with the measured data, and the relative magnitude and position of the side lobes agree satisfactorily up to the high background in the measured data. In contrast, the theoretical description and measured scattering do not match for the shorter lengths; in particular, for $l = 6$ μm (Fig. 4b), the measured FWHM is much smaller than expected and a second peak is measured at $\alpha_f \simeq 0.45°$. The reason for the mismatch at the shortest line lengths is that slow intensity variations in the k_z direction along the grating truncation sheets become visible when the width of the slit diffraction becomes large enough. As can be seen in Fig. 3(b), the elongated diffraction orders cut the grating truncation sheets along k_z, and the shorter the grating, the larger is the probed q_z-window. From previous studies (Suh et al., 2016; Soltwisch et al., 2017) on practically infinitely long gratings, it is known that the intensity of the grating diffraction orders at different q_z depends on the exact line profile, with the main effect being an intensity oscillation with period $\Delta q_z = 2\pi/h$ with the height of the grating lines h. For the nominal line height of $h = 45$ nm, the height oscillation is therefore expected with a period of $\Delta\alpha_f \simeq 0.26°$, which agrees with the distance between the two peaks seen in Fig. 4(c) of $\Delta\alpha_f \simeq 0.18°$. For longer line lengths and thus sharper effective slit diffraction, the height oscillation is too broad to have a large effect on the measured FWHM, but for smaller line lengths and broader effective slit diffraction the height oscillation will lead to an inner structure in the main slit diffraction peak. By extracting the FWHM without regard for the inner structure, for most measurements the deviation between measured and predicted FWHM is minimized. However, for $l = 6$ μm, the deviation is large because the small peak at $\alpha_f \simeq 0.45°$ does not contribute to the measured FWHM.

5. Surrounded small fields

In most cases, small targets are not isolated on a blank wafer. Therefore, it is essential to separate the parasitic scattering of the surroundings from the scattering of the target structure. Assuming incoherent addition, we can separate the scattering by describing the individual contributions. One way to separate the scattering of the target and the surroundings if both the target and the surroundings are oriented internally would be a variation of the dominant length scale (for gratings, the pitch p) of the target with respect to the surroundings, which would lead to a separation in θ_f. However, the sensitivity of θ_f to changes in p is not very high, and for surroundings with multiple dominant length scales it might be difficult to find a suitable p for the target. Therefore, it is advantageous to rotate the target in the sample plane with respect to the surroundings, which leads to a separation of the scattering in α_f. If the surroundings and the target can be described in good approximation as gratings, this effect can be quantified using equation (4).
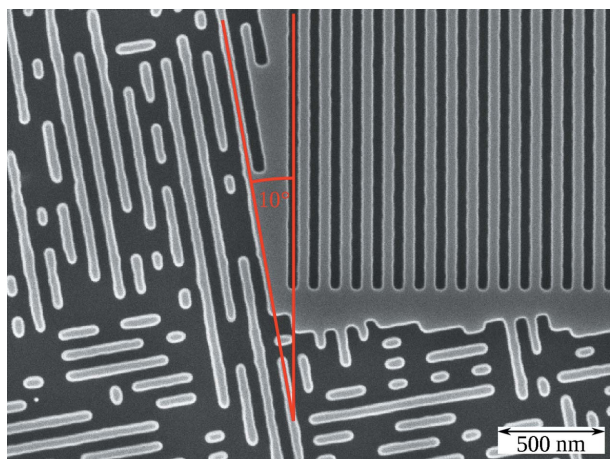
Figure 5
Top-view SEM image of surrounded field 1, showing the corner of the small grating field (top right) and the surroundings. Darker areas correspond to etched grooves, lighter areas to mesas. The orientations of the small grating field and the surroundings, at 10° rotation, are in red.

To show a GISAXS measurement of small targets in structured surroundings, we manufactured small grating targets surrounded by ordered but randomized structures, with the grating orientation rotated by 10° with respect to the orientation of the surroundings (see Fig. 5). To explore the sensitivity of GISAXS measurements of small grating targets to changes in the target line profile, we manufactured two targets with differing line widths but identical surroundings. The surroundings measured 100 μm × 100 μm and the grating targets at the centre of the surroundings measured

15 μm × 15 μm. For both targets, the surroundings consisted of boxes with randomized lengths between 0.2 μm and 3 μm, oriented either in parallel or orthogonally to the standard beam direction. Both grating targets had a grating pitch of $p =$ 100 nm and a nominal line height of $h = $ 100 nm, but differed in the line width w. For surrounded field 1, the line width was $w = 45$ nm and for surrounded field 2 it was $w = 55$ nm.

GISAXS measurements of the surrounded fields were taken with a beam size of 0.1 mm × 0.1 mm, such that the width of the X-ray beam corresponded to the width of the surroundings. Measurements were taken at different sample rotations φ; the results are shown in Fig. 6. The scattering contributions of the surroundings and the target are well separated and follow the theoretical expectation. Although the target only covers about 2.3% of the structured area, only the scattering of the target is visible on the detector if the beam is aligned with the target. Due to the high sensitivity of the exit angle α_f to small deviations in the rotation φ, the grating diffraction orders of the surroundings as well as the diffuse halo originating from the surroundings are suppressed when measuring in the target direction, as can be seen by the absence of scattering originating from the surroundings if the beam is aligned just between the target and the surroundings ($\varphi = -5°$).

We measured target GISAXS patterns ($\varphi = 0°$) at photon energies from $E = 5750$ eV up to $E = 6250$ eV for both surrounded field 1 (line width $w = 45$ nm) and surrounded field 2 ($w = 55$ nm). Vertical cuts through the second diffraction order (at $q_y = 0.126$ nm^{-1}) for both targets and all energies are shown in Fig. 7. The measurements can be understood in terms of the reciprocal-space construction. Within this framework,
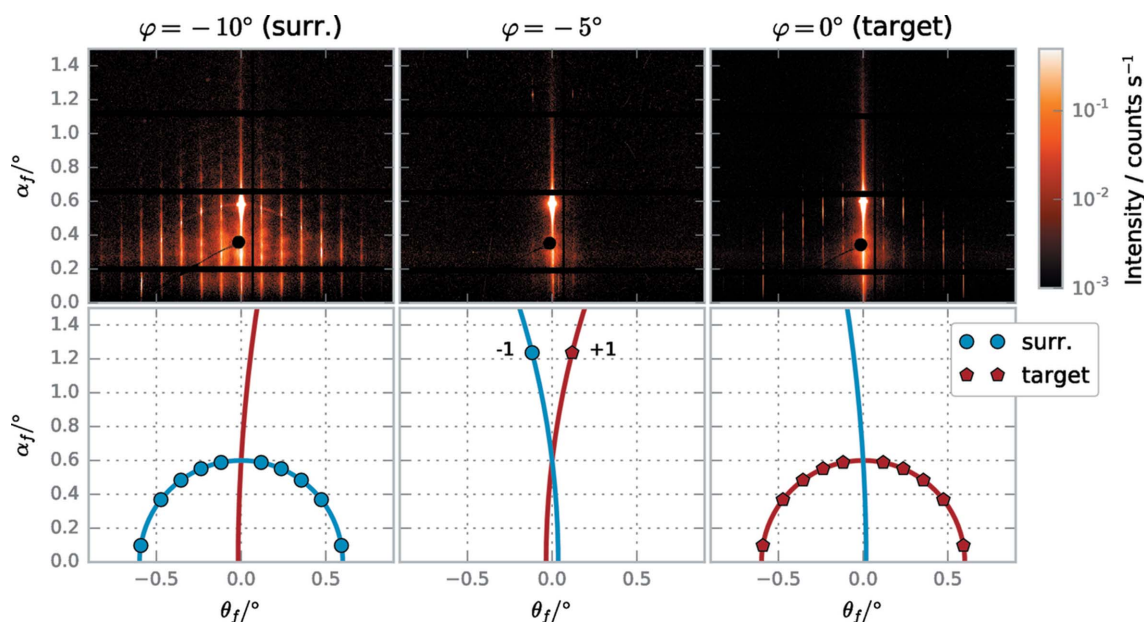

Figure 6
GISAXS measurements (upper row) *versus* theoretical expectation (lower row) of surrounded field 1 at different rotation angles φ. At $\varphi = -10°$ (left) the X-ray beam is oriented along the surrounding structure, showing the scattering orders of the surroundings and a rich diffuse background. At $\varphi = -5°$ (middle) the X-ray beam is equally misaligned to the surroundings and the grating target, with only the first diffraction order visible at $\alpha_f \simeq 1.2°$ for the surroundings and the target, respectively. With the X-ray beam aligned to the target ($\varphi = 0°$, right), only the scattering of the target is visible on the detector. An animated sequence showing scattering patterns from $\varphi = -10°$ to $\varphi = 0°$ in steps of $\Delta\varphi = 0.1°$ is available in the supporting information.
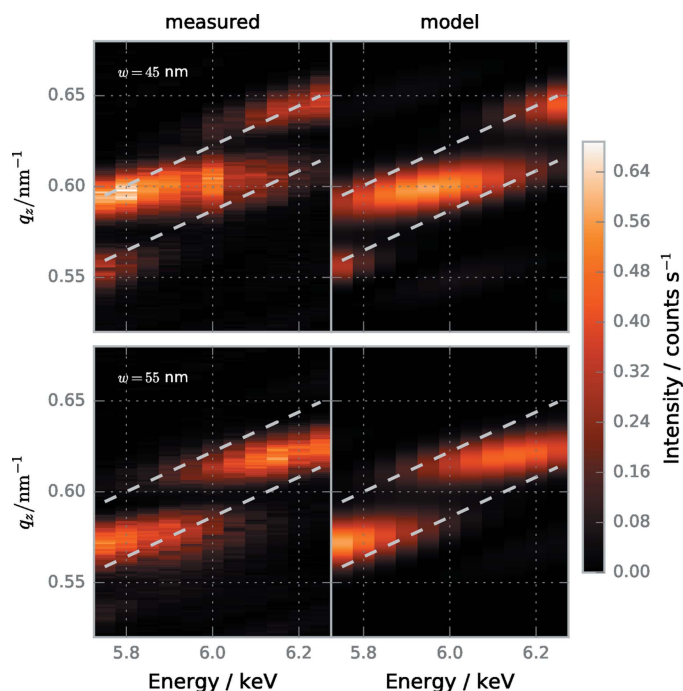
Figure 7
Vertical cuts through the second diffraction order of the GISAXS patterns collected at different photon energies (measured data on the left, fitted model on the right). The measurements for surrounded field 1 (line width $w = 45$ nm, top) and for surrounded field 2 ($w = 55$ nm, bottom) are shown. The dashed lines show the FWHM of the slit diffraction calculated using equation (7), which indicates the window of reciprocal space measured at the respective photon energy. Since detector quantum efficiency and photon flux change with the photon energy, absolute intensities are not comparable between different photon energies.

changing the photon energy alters the radius of the Ewald sphere and consequently the position of the intersection between the Ewald sphere and the grating truncation sheets. Effectively, we measure a different part of the grating truncation sheets at each energy, explaining why the cuts show zero intensity outside of this window into reciprocal space. The intensity profile within the measured window then depends on intensity variations in the k_z direction (mainly the height oscillations) as explained in the discussion of deviations between theoretical expectation and measurements for the smallest line lengths in the previous section. To show that the intensity variations along q_z explain the measurements, we use a model composed of an intensity distribution $I_z(q_z)$ which does not change with photon energy multiplied with the energy-dependent slit diffraction according to equation (6). As a first approximation for I_z, we use Gaussian peaks. Fig. 7 shows models fitted to the data using the known length $l = 15$ µm for the slit diffraction and three or, respectively, two Gaussian peaks for $w = 45$ nm and $w = 55$ nm. While relative intensities are not accurately represented, the models describe peak positions very well, showing that the intensity profile within the measured window is explained by target features in the z-direction. The distance between the peaks is about $\Delta q_z = 0.5$ nm^{-1}, which roughly corresponds to the nominal line height of $h = 100$ nm in real space along z. Comparing the

measurements for the two targets with different line widths, Δq_z does not change significantly, but the position of the peaks is shifted. From previous studies (Suh *et al.*, 2016; Soltwisch *et al.*, 2017), it is known that the intensity of the non-elongated grating diffraction orders depends on the exact line profile. We therefore attribute the changes in position and relative intensity of the observed peaks within the elongated diffraction orders to the differences in line profile, mainly the differing line widths.

6. Conclusions

We have shown that even with millimetre-sized beams, which are available at many synchrotron and laboratory-based X-ray sources, micrometre-sized targets can be measured. The minimum target sizes which were investigated are an order of magnitude smaller than the smallest micro-beam footprints which have been used in GISAXS experiments so far (Roth *et al.*, 2007). The challenge in the measurements is separating the scattering signal of the target from the scattering of its surroundings. While this separation is easily done for trivial surroundings like a bare substrate, it becomes more challenging if the scattering of structured surroundings and the target overlap. We managed to separate the scattering of periodic targets in nanostructured surroundings if the targets were rotated with respect to the predominant direction of the surroundings.

The presented formulae for single-slit diffraction describe the elongation of grating diffraction orders and the appearance of side lobes when going from effectively infinite to short targets. A comparison of the scattering of two small grating targets with different line widths shows that GISAXS measurements of small targets are sensitive to the grating line profile. By scanning the photon energy, the scattering intensity along the grating truncation rods could be obtained, which will enable extraction of relevant structural parameters of the gratings if the scattering can be described theoretically. For infinitely long grating lines, previous studies using the DWBA (Suh *et al.*, 2016) or a Maxwell solver (Soltwisch *et al.*, 2017) reduced the calculations of GISAXS measurements to two dimensions and were then able to reconstruct the full line profile. As short lines are inherently three-dimensional, further research is needed to extend these methods to the reconstruction of line profiles of short grating targets.

Using the techniques described in this paper, it is possible to employ GISAXS, with its distinct advantages, for applications such as characterization of metrology fields in the semiconductor industry where up to now it has been considered impossible due to the large beam footprint.

patent claiming inventions partly described in this paper (Soltwisch & Pflüger, 2017).

References

Babonneau, D., Camelio, S., Lantiat, D., Simonot, L. & Michel, A. (2009). *Phys. Rev. B*, **80**, 155446.

Beckhoff, B., Gottwald, A., Klein, R., Krumrey, M., Müller, R., Richter, M., Scholze, F., Thornagel, R. & Ulm, G. (2009). *Phys. Status Solidi B*, **246**, 1415–1434.

Bunday, B. (2016). *Proc. SPIE*, **9778**, 97780E.

Fuchs, D., Krumrey, M., Müller, P., Scholze, F. & Ulm, G. (1995). *Rev. Sci. Instrum.* **66**, 2248–2250.

Gleber, G., Cibik, L., Haas, S., Hoell, A., Müller, P. & Krumrey, M. (2010). *J. Phys. Conf. Ser.* **247**, 012027.

Gollmer, D. A., Walter, F., Lorch, C., Novák, J., Banerjee, R., Dieterle, J., Santoro, G., Schreiber, F., Kern, D. P. & Fleischer, M. (2014). *Microelectron. Eng.* **119**, 122–126.

Gu, Y., Wang, C. & Russell, T. P. (2012). *Adv. Energ. Mater.* **2**, 683–690.

Hexemer, A. & Müller-Buschbaum, P. (2015). *IUCrJ*, **2**, 106–125.

Hlaing, H., Lu, X., Hofmann, T., Yager, K. G., Black, C. T. & Ocko, B. M. (2011). *ACS Nano*, **5**, 7532–7538.

Hofmann, T., Dobisz, E. & Ocko, B. M. (2009). *J. Vac. Sci. Technol. B*, **27**, 3238.

Holý, V. & Baumbach, T. (1994). *Phys. Rev. B*, **49**, 10668–10676.

Holý, V., Kuběna, J., Ohlídal, I., Lischka, K. & Plotz, W. (1993). *Phys. Rev. B*, **47**, 15896–15903.

Hu, T., Jones, R. L., Wu, W., Lin, E. K., Lin, Q., Keane, D., Weigand, S. & Quintana, J. (2004). *J. Appl. Phys.* **96**, 1983–1987.

Jergel, M., Mikulík, P., Majková, E., Luby, Š., Senderák, R., Pinčík, E., Brunel, M., Hudek, P., Kostič, I. & Konečníková, A. (1999). *J. Appl. Phys.* **85**, 1225–1227.

Krumrey, M. & Ulm, G. (2001). *Nucl. Instrum. Methods Phys. Res. A*, **467–468**, 1175–1178.

Lairson, B. M., Payne, A. P., Brennan, S., Rensing, N. M., Daniels, B. J. & Clemens, B. M. (1995). *J. Appl. Phys.* **78**, 4449–4455.

Levine, J. R., Cohen, J. B., Chung, Y. W. & Georgopoulos, P. (1989). *J. Appl. Cryst.* **22**, 528–532.

Meier, R., Chiang, H.-Y., Ruderer, M. A., Guo, S., Körstgens, V., Perlich, J. & Müller-Buschbaum, P. (2012). *J. Polym. Sci. B*, **50**, 631–641.

Meschede, D. (2015). *Gerthsen Physik*, Springer-Lehrbuch, pp. 533–583. Berlin/Heidelberg: Springer.

Metzger, T. H., Haj-Yahya, K., Peisl, J., Wendel, M., Lorenz, H., Kotthaus, J. P. & Cargill, G. S. III (1997). *J. Appl. Phys.* **81**, 1212–1216.

Mikulík, P. & Baumbach, T. (1999). *Phys. Rev. B*, **59**, 7632–7643.

Mikulík, P., Jergel, M., Baumbach, T., Majková, E., Pincik, E., Luby, S., Ortega, L., Tucoulou, R., Hudek, P. & Kostic, I. (2001). *J. Phys. D*, **34**, A188.

Müller-Buschbaum, P. (2003). *Anal. Bioanal. Chem.* **376**, 3–10.

Müller-Buschbaum, P. (2014). *Adv. Mater.* **26**, 7692–7709.

Pröller, S., Liu, F., Zhu, C., Wang, C., Russell, T. P., Hexemer, A., Müller-Buschbaum, P. & Herzig, E. M. (2016). *Adv. Energ. Mater.* **6**, 1501580.

Renaud, G., Lazzari, R. & Leroy, F. (2009). *Surf. Sci. Rep.* **64**, 255–380.

Renaud, G., Lazzari, R., Revenant, C., Barbier, A., Noblet, M., Ulrich, O., Leroy, F., Jupille, J., Borensztein, Y., Henry, C. R., Deville, J.-P., Scheurer, F., Mane-Mane, J. & Fruchart, O. (2003). *Science*, **300**, 1416–1419.

Rossander, L. H., Zawacka, N. K., Dam, H. F., Krebs, F. C. & Andreasen, J. W. (2014). *AIP Adv.* **4**, 087105.

Roth, S. V., Autenrieth, T., Grübel, G., Riekel, C., Burghammer, M., Hengstler, R., Schulz, L. & Müller-Buschbaum, P. (2007). *Appl. Phys. Lett.* **91**, 091915.

Rueda, D. R., Martín-Fabiani, I., Soccio, M., Alayo, N., Pérez-Murano, F., Rebollar, E., García-Gutiérrez, M. C., Castillejo, M. & Ezquerra, T. A. (2012). *J. Appl. Cryst.* **45**, 1038–1045.

Senn, T., Bischoff, J., Nüsse, N., Schoengen, M. & Löchel, B. (2011). *Photon. Nanostruct.* **9**, 248–254.

Soccio, M., Rueda, D. R., García-Gutiérrez, M. C., Alayo, N., Pérez-Murano, F., Lotti, N., Munari, A. & Ezquerra, T. A. (2015). *Polymer*, **61**, 61–67.

Soltwisch, V., Fernández Herrero, A., Pflüger, M., Haase, A., Probst, J., Laubis, C., Krumrey, M. & Scholze, F. (2017). Submitted.

Soltwisch, V. & Pflüger, M. (2017). Verfahren zur Qualitätssicherung einer Belichtungsmaske und Belichtungsmaske (German Patent application).

Soltwisch, V., Wernecke, J., Haase, A., Probst, J., Schoengen, M., Krumrey, M. & Scholze, F. (2014a). *Proc. SPIE*, **9050**, 905012.

Soltwisch, V., Wernecke, J., Haase, A., Probst, J., Schoengen, M., Krumrey, M., Scholze, F., Pomplun, J. & Burger, S. (2014b). *Proc. SPIE*, **9235**, 92351D.

Suh, H. S., Chen, X., Rincon-Delgadillo, P. A., Jiang, Z., Strzalka, J., Wang, J., Chen, W., Gronheid, R., de Pablo, J. J., Ferrier, N., Doxastakis, M. & Nealey, P. F. (2016). *J. Appl. Cryst.* **49**, 823–834.

Sunday, D. F., List, S., Chawla, J. S. & Kline, R. J. (2015). *J. Appl. Cryst.* **48**, 1355–1363.

Tolan, M., Press, W., Brinkop, F. & Kotthaus, J. P. (1995). *Phys. Rev. B*, **51**, 2239–2251.

Wernecke, J., Gollwitzer, C., Müller, P. & Krumrey, M. (2014c). *J. Synchrotron Rad.* **21**, 529–536.

Wernecke, J., Okuda, H., Ogawa, H., Siewert, F. & Krumrey, M. (2014a). *Macromolecules*, **47**, 5719–5727.

Wernecke, J., Scholze, F. & Krumrey, M. (2012). *Rev. Sci. Instrum.* **83**, 103906.

Wernecke, J., Shard, A. G. & Krumrey, M. (2014b). *Surf. Interface Anal.* **46**, 911–914.

Yan, M. & Gibaud, A. (2007). *J. Appl. Cryst.* **40**, 1050–1055.